Conductive *In Situ* Reduced Graphene Oxide−Silk Fibroin Bionanocomposites

Parushuram Nilogal, Gauthama B. Uppine, Ranjana Rayaraddi, Harisha K. Sanjeevappa, Lavita J. Martis, Badiadka Narayana, and Sangappa Yallappa*

Read Online

ACCESS | Metrics & More | Article Recommendations

ABSTRACT: This research paper describes the fabrication of bionanocomposites (BNCs) based on silk fibroin (SF) and reduced graphene oxide (rGO). The recorded UV−visible (UV−vis) spectra of the sample confirm the reduction of GO to rGO in SF by showing a plasmon resonance band within the wavelength range of 261−268 nm. The X-ray diffraction (XRD) peak at 11.6° corresponding to the GO intensity decreases with increasing reaction time, resulting in rGO in the SF host matrix. The morphological behavior of the SF−rGO BNCs is scrutinized using scanning electron microscopy (SEM), and the images clearly indicate the existence of rGO within the matrix. The increasing amount of GO in the SF shows broken graphene sheets, which can increase the surface roughness and establish a strong physical contact between the SF and rGO nanosheets. The high-resolution transmission electron microscope (HR-TEM) image of the bionanocomposite showed that the formed rGO encompassments of fewer layers are stacked, each with fewer wrinkles and folding. The Raman spectroscopy confirmed the formation of rGO by showing the increased intensity ratio of D to G band (I_D/I_G) in the bionanocomposite samples. The rGO effect on the electrical conductivity is measured, and the results show that DC conductivity increases from 1.28×10^{-9} to 82.4×10^{-9} S/cm with an increase in the GO content in the SF biopolymer. The investigations demonstrate loss of the insulation property and improved conducting behavior of the SF biopolymer.
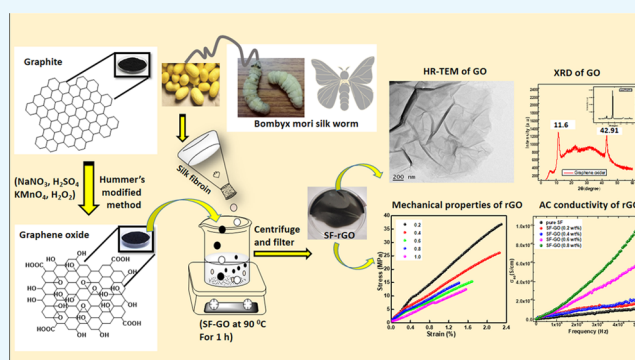
1. INTRODUCTION

The silk obtained from domesticated silkworm (*Bombyx mori*) is a semicrystalline natural biopolymer and has received considerable attention for nontextile applications in recent years.[1] The protein macromolecule is explored as a technologically useful material and is employed in different fields.[2] Silk is primarily made up of two important protein constituents, namely, silk fibroin (SF) and sericin. Silk fibroin is the core of the fiber, and sericin is a binding material that holds the fibroin fibers together.[3]

In recent years' research, SF has proved to be a very popular and useful stuff in biomedical fields because of its extraordinary mechanical strength, biocompatibility, biodegradability, nontoxicity, favorable oxygen and water permeability, and nominal inflammatory reaction.[4] Additionally, SF offers versatility in processing so that it can be easily fabricated into porous scaffolds, microspheres, films, gels, fibers, and powder form for different uses.[5−8] Its multifunctional features and process ability help the selection of SF for extensive use in areas of wound healing,[9] optics, optoelectronics, and photonics.[10] Free-standing SF films are widely prepared and used in luminescent solar concentrators, optical devices, electrical conduction and dielectric relaxation, and several other fields.[11−13]

In the literature, the avenue was made in the field of sensors by introducing some nanomaterials for non-enzymatic glucose sensing[14] and SERS nanosensor-enabled long-term *in vivo* glucose tracking.[15] Also, biopolymers and polymer composites have been used as body motion sensors,[16] temperature sensors,[17] and piezoelectric sensors.[18] In addition, a few studies have reported piezoresistive sensors based on the SF polymer composite, which are found to be very useful for force and deformation measurements.[19] However, native SF is insulating in nature, and in wet condition, shows very poor electrical properties.[20] To improve its electrical conductivity, it is essential to combine it with some conductive materials like ionic liquids,[21] conducting polymers,[22] and carbon-based
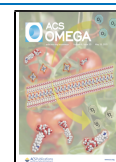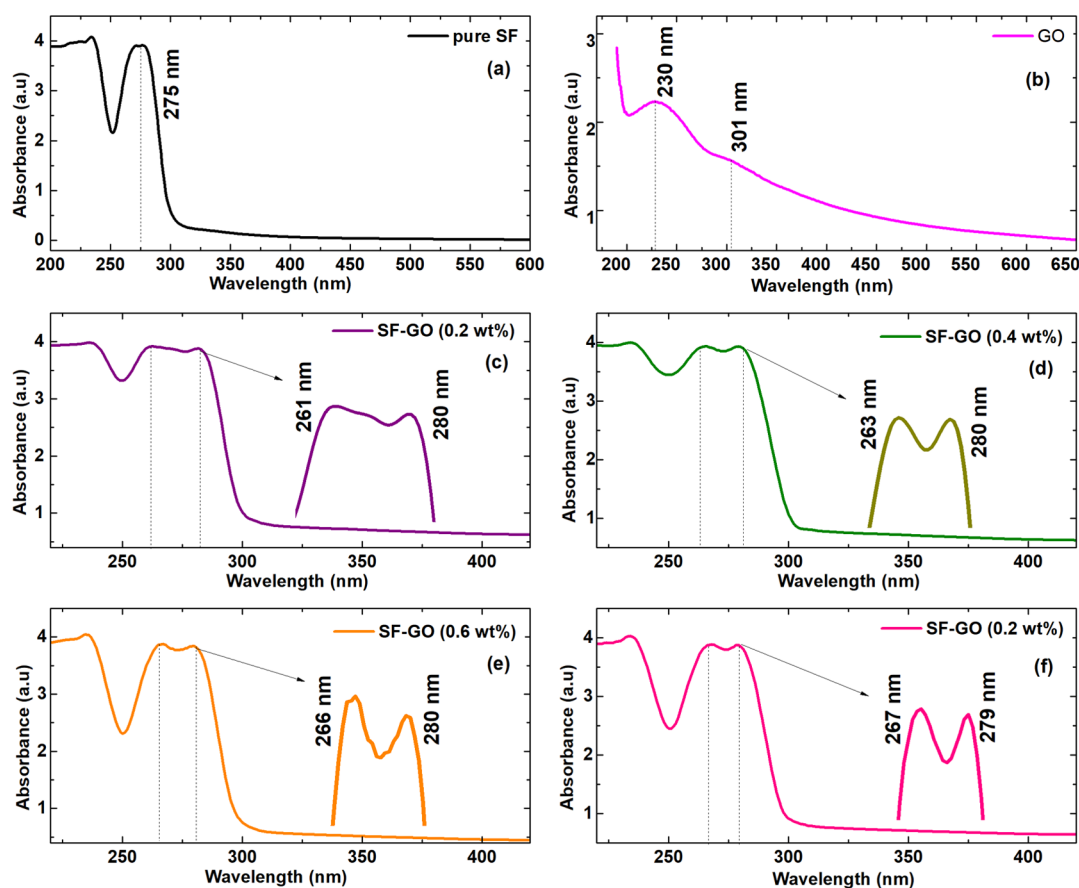
Figure 1. UV−visible absorption spectra of SF−rGO nanocomposites. (a) SF, (b) GO, (c) SF−GO (0.2 wt %), (d) SF−GO (0.4 wt %), (e) SF−GO (0.6 wt %), and (f) SF−GO (0.8 wt %).

materials for the fabrication of conductive SF composites.[23] The nanocomposite normally consists of a polymer with conductive fillers,[24] of which one of the constituents has dimensions in the nanoscale (<100 nm). Normally, polymerization is a modest approach for combining different materials so as to overcome the deficient properties of a material.[25]

In the present work, an SF−rGO bionanocomposite was fabricated via *in situ* reduction of GO to reduced GO nanosheets in the SF. The developed nanocomposite comprises an organic material (silk fibroin) and inorganic reduced GO nanosheet components. Graphene oxide is one of the carbon materials that has gained considerable interest in recent years. GO is a form of graphene having various oxygen-containing functional groups, induces stable dispersion in many polar and nonpolar substances, including water, and is thus widely used in many industrial applications for benefits different from those of native graphene.[26−28] Because of the presence of oxygen-containing functional groups, graphene oxide has good thermal, electrical, and mechanical properties[29−31] due to its 2D sp[2] carbon honeycomb structure. It is well reported in the literature that the functional groups can be removed to obtain stable graphene, which is called reduced graphene oxide (often abbreviated to rGO).[32,33] Few studies have documented the composite of a graphene oxide hybrid that can be used as a bifunctional catalyst for hydrogen evolution and hydrogen storage,[34] asymmetric supercapacitors,[35,36] electrochemical supercapacitors,[37] self-healing polymer composites,[38] as anode material for lithium-ion batteries,[39] EMI shielding,[40−42] and in graphene and graphene oxide-based

membranes for gas separation.[43,44] Also, graphene nanofillers were synthesized and incorporated into starch to improve its mechanical properties and long-term stability.[45] The present report demonstrates SF as a biomaterial that can be used to reduce GO to rGO and fabricate the SF−rGO bionanocomposite. This may offer a broad spectrum of new advantages for a large variety of environmentally friendly sensors, photonics, electronics, biotechnology, and medical applications. Different analytical instruments like UV−vis spectroscopy, XRD, SEM, TEM, mechanical tests, Raman spectroscopy, TGA, and XPS were employed to characterize the fabricated SF−rGO BNCs. The electrical properties of the bionanocomposite were also evaluated, and the results are discussed in the paper.

2. RESULTS AND DISCUSSION

2.1. UV−Visible Spectroscopy Analysis. The attainment of reduced GO from GO using the biopolymer *B. mori* SF was studied by UV−vis spectroscopy. The UV−vis optical absorption plots of the native SF, GO, and SF−rGO bionanocomposite were recorded and are presented in Figure 1. The native SF displayed an absorption peak at wavelength λ = 275 nm due to the $\pi \rightarrow \pi^*$ transition of the tyrosine residue in the SF macromolecule.[46] On the other hand, the synthesized GO sample exhibited two absorption peaks at λ_1 = 230 nm, which can be ascribed to the $\pi \rightarrow \pi^*$ of the C═C Plasmon peak. Another shoulder peak observed around λ_2 = 300 nm corresponds to the n $\rightarrow \pi^*$ transition of the carbonyl groups.[47] In the composites, after adding GO to the SF, it was found that the plasmon peak observed at 230 nm slowly red-shifts to 268

nm. As the reduction time and amount of GO are increased in the host matrix, this peak becomes prominent and a slight increase in intensity is observed. This reflects increased π-electron concentration and structural ordering, which is similar to the restoration of sp[2] carbon and possible rearrangement of the atoms.[25] It indicates that the GO might have reduced successfully, and the degree of reduction improves with the increase of the reaction time and the GO in the SF. Therefore, the UV-absorption spectra of the BNCs (Figure 1c−f) exhibit two absorption peaks at λ = 268 and 280 nm, which can be attributed to the reduced GO (rGO) and SF, respectively. The distinctive peak observed at λ = 268 nm confirms the formation of rGO in the host matrix. It is also observed that the characteristic absorption peak of Tyr at 275 nm decreases slightly and red-shifts to 280 nm. The shifting of the Tyr peak may be because of the transfer of electrons from the Tyr to the GO altering the electron configuration in the Tyr moiety in the process of reduction. The possible mechanism is discussed in Section 2.2 (Scheme 1).

Scheme 1. Possible Mechanism
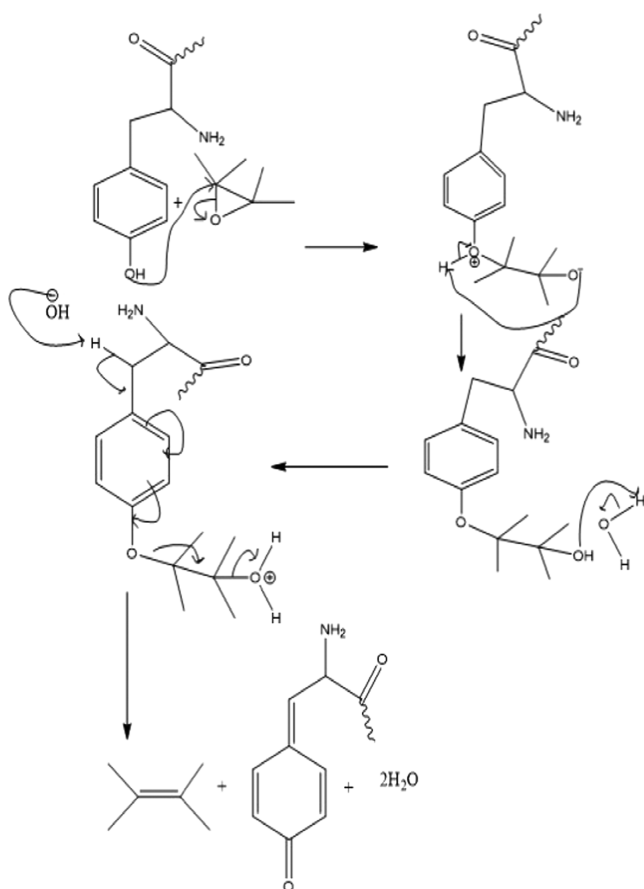
2.2. XRD Analysis. X-ray diffraction measurements were carried out to evaluate the structures of the native SF, GO, and SF−rGO bionanocomposites. The recorded XRD scans of the samples are given in Figure 2. From the XRD scan (Figure 2a), it can be noticed that the characteristic main diffraction peak (002) of raw graphite was detected at a scattering angle $2\theta = 26.5°$. This corresponds to an interlayer d-spacing of 0.338 nm.[49] On the other hand, the main characteristic diffraction peak of the synthesized GO was observed at $2\theta = 11.6°$ (Figure 2b) corresponding to a d-spacing of 0.78 nm.[48] The larger

interlayer spacing of GO may be due to the generation of oxygen-containing functional groups because of the oxidation of graphite.[49] Earlier studies on native SF showed that the characteristic diffraction peaks corresponding to the silk-I structure are at 12.2, 19.7, 24.7, and 28.2°, and for the silk-II structure are at 9.1, 18.9, 20.7, and 24.3°.[50] The recorded SF film (Figure 2c) displays diffraction peaks at scattering angles $2\theta = 9.41, 12.16, 19.64, 24.34,$ and $28.71°$, confirming the existence of the crystalline domains of both silk-I and silk-II structures. When the GO is added into the SF, the XRD scans of the BNCs show SF and GO diffraction peaks. With the increase of GO content in the SF and the reaction time, the diffraction peak $2\theta = 11.6°$ corresponding to GO slowly decreases, and at the highest concentration, the intensity is seen to be diminished. In comparison with pure SF, the intensity of the silk-II or β-sheet diffraction peak at 24.3° is increased, and another peak at 20.5°, attributed to the silk-II structure, appeared progressively as the GO content was increased. Thus, the XRD study clearly confirms that GO reduction can be enhanced significantly to produce rGO nanosheets in the SF solution by increasing the reaction time.

2.3. SEM Analysis. The surface morphologies of native SF, GO, and BNCs with different contents of GO nanosheets were studied using SEM, and the images are depicted in Figure 3. The SEM images (Figure 3a,b) of the pure SF sample are very clean and smooth, and the GO shows a layered structure with relatively neat orientation,[51] whereas the SEM images of the BNCs (Figure 3c−f) clearly admit the dispersion of the GO in the host polymer. The *in situ* formed reduced GO nanosheets are well distributed throughout the samples. The increasing amount of rGO content shows broken graphene sheets in the host matrix, which can increase the surface roughness of the BNCs. It could establish strong linkage between the host and the rGO nanosheets. This can greatly reduce the insulation property of the SF and considerably increase the electric conductivity behavior of the BNC samples.[52]

2.4. TEM Analysis. Figure 4a,b depicts high-resolution transmission electron microscopy images of the synthesized GO, which exhibit typical wrinkle and folded morphology. From Figure 4a,b, it can be noted that the GO is very thin and shows a translucent sheet structure.[53] These images are used to detect the number of layers and structural morphology. The folding of one or two layers at the edges of the films appears as dark lines. The HR-TEM images of the bionanocomposite are illustrated in Figure 5a. The obtained image showed that the rGO encompassments of fewer layers are stacked, each with lesser wrinkles and folding. The implanted image in Figure 5a is a crystallographic structure of the graphene sheet and was characterized by the selected area electron diffraction (SAED) method, which exhibited a single set of hexagonal diffraction patterns with sharp and clear diffraction spots. Figure 5b clearly shows the lattice fringes, which provide supplementary evidence regarding the interplanar distance d_{002} (0.36 nm).

2.5. Mechanical Properties of BNCs. Mechanical properties are crucial for assessing the BNCs for different applications. For the assessment of the mechanical properties of the developed BNCs, mechanical tests were conducted. Figure 6 illustrates the stress−strain curves of the native SF and BNCs with varying GO content in the host matrix. Mechanical properties like tensile strength (TS in MPa), elongation at break (%), and Young's modulus (YM in MPa) of the samples were calculated using the stress−strain curves acquired in dry
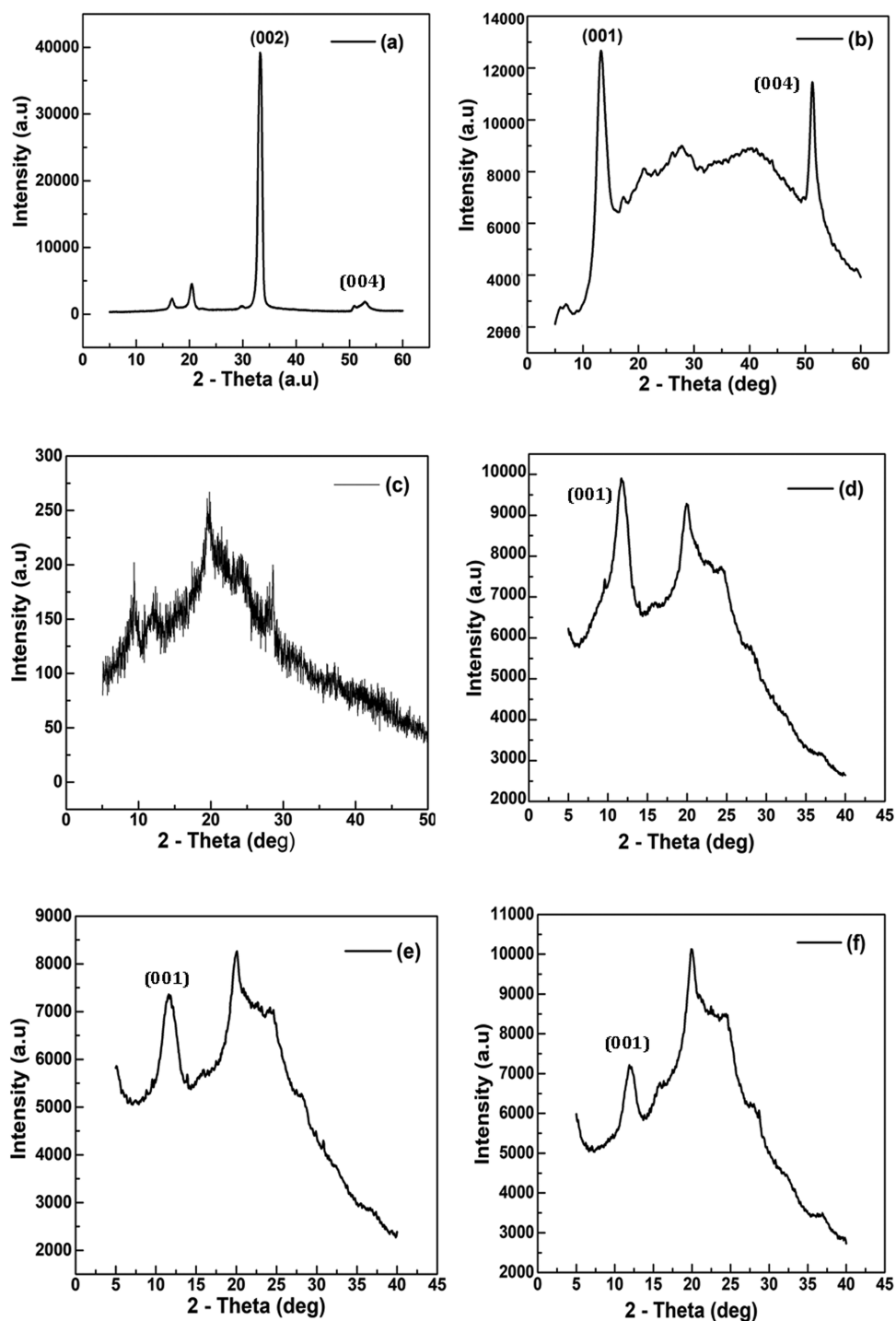
Figure 2. XRD scans of (a) graphite powder, (b) graphene oxide powder, (c) pure SF, (d) SF−rGO (0.4 wt % GO), (e) SF−rGO (0.6 wt % GO), and (f) SF−rGO (0.8 wt % GO) bionanocomposites.

state. The tensile strength (TS in MPa) of the samples was calculated using the following relation[54]

$$TS = \frac{F_{max}}{A} \qquad (1)$$

where F_{max} indicates the maximum load-bearing capacity of the films at the moment of breaking (N) and A shows the cross-sectional area of the samples (i.e., thickness × width). The percentage of elongation at break (E in %) was calculated using the following relation

$$E(\%) = \frac{\Delta L}{L_0} \times 100 \qquad (2)$$

where L_0 indicates the initial length of the films or gauge length (50 mm) and ΔL shows the change in length of the sample at the stage of break. The Young's modulus (YM) of the measured samples, which is inversely proportional to the elasticity, can be obtained from the initial slope of the curves. The calculated mechanical properties of the samples are given in Table 1. From Table 1, it can be observed that the TS of the native SF film is 37.0 ± 0.655 MPa, YM is 2070 ± 0.588 MPa,
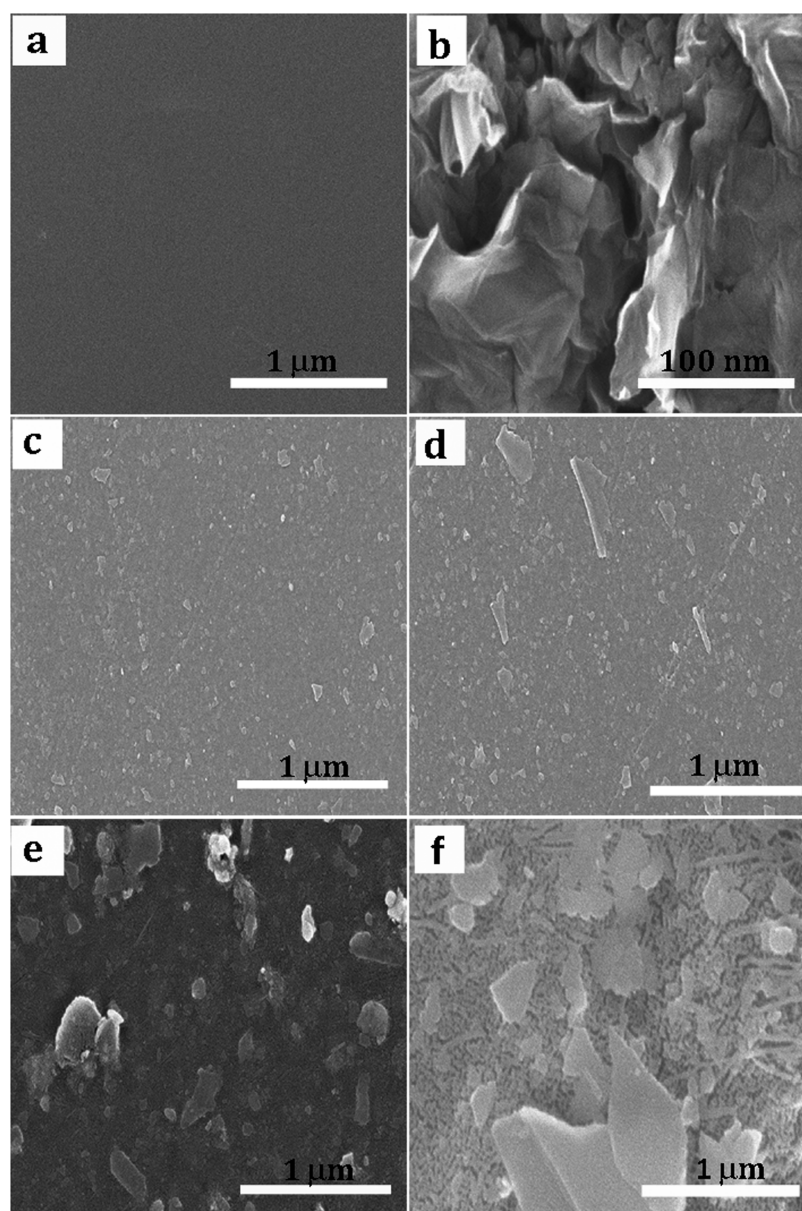
Figure 3. SEM images of SF−rGO bionanocomposite films. (a) pure SF, (b) GO, (c) SF−rGO (0.2 wt % GO), (d) SF−rGO (0.4 wt % GO), (e) SF−rGO (0.6 wt % GO), and (f) SF−rGO (0.8 wt % GO).
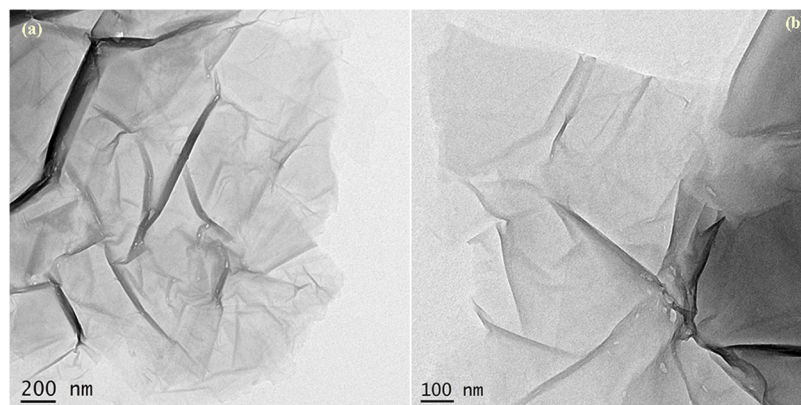
Figure 4. HR-TEM images of GO nanosheets of (a) scale 200 nm and (b) scale 100 nm.

and elongation at break is 2.3 ± 0.076%. In case of the 0.2 wt % GO-added SF sample, the TS value is 26.2 ± 0.208 MPa and YM is 1620 ± 0.736 MPa. For the highest concentration (0.8 wt % GO), the TS is 12.5 ± 0.100 MPa and YM is 667 ± 0.697
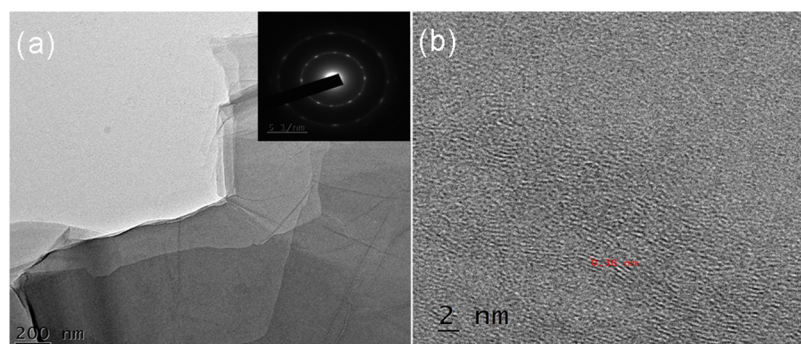
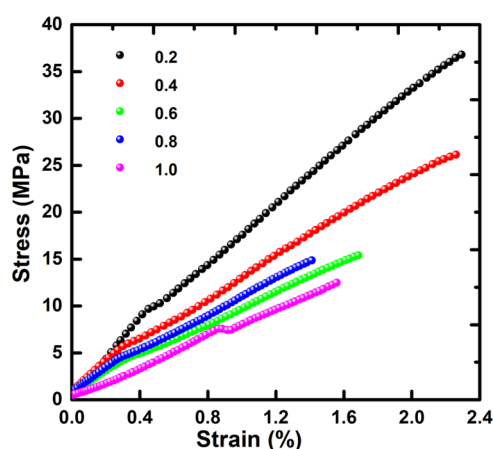**Figure 5.** (a) HR-TEM images of rGO nanosheets; (b) HR-TEM micrograph of rGO.

Figure 6. Stress−strain curves of SF and SF−rGO bionanocomposites.

Figure 7. TGA scans. (a) SF, (b) GO, (c) SF−rGO (0.2 wt % GO), (d) SF−rGO (0.4 wt % GO), (e) SF−rGO (0.6 wt % GO), and (f) SF−rGO (0.8 wt % GO) bionanocomposites.

Table 1. Mechanical Properties of SF and SF−GO BNC Films

samples	tensile modulus (MPa)	tensile strength (MPa)	elongation break (%)
SF	2070 ± 0.588	37.0 ± 0.655	2.3 ± 0.076
SF + 0.2 wt % GO	1620 ± 0.736	26.2 ± 0.208	2.3 ± 0.010
SF + 0.4 wt % GO	1180 ± 0.555	15.5 ± 0.251	1.7 ± 0.010
SF + 0.6 wt % GO	1320 ± 0.524	15.0 ± 0.060	1.4 ± 0.020
SF + 0.8 wt % GO	0667 ± 0.697	12.5 ± 0.100	1.6 ± 0.010

MPa. It was observed that the mechanical behavior of the SF−rGO bionanocomposites deteriorated with the increase in GO content in the SF. Particularly, the TS and YM of the SF−rGO bionanocomposites decreased with increase in GO loading from 0 to 0.8 wt % in the host matrix. The elongation at break also decreased with increasing content of the GO. Thus, the interaction between the SF and GO nanosheets and the reduction of GO restrict the free movement of the SF chains. Moreover, the silk-II structure, which could be stiffer, is more brittle in nature.[50]

2.6. Thermogravimetric Analysis. Thermogravimetric analysis was performed to understand the effect of GO on the thermal stability of the SF−rGO bionanocomposites. The recorded TGA scans of the native SF, GO, and SF−rGO samples are illustrated in Figure 7a−f. All of the samples show three stages of weight loss. For the native SF, the initial weight loss was about (Figure 7a) ∼10%, which took place from laboratory temperature to 105 °C, showing the evaporation of the water vapor molecules in the sample.[55] The next stage of
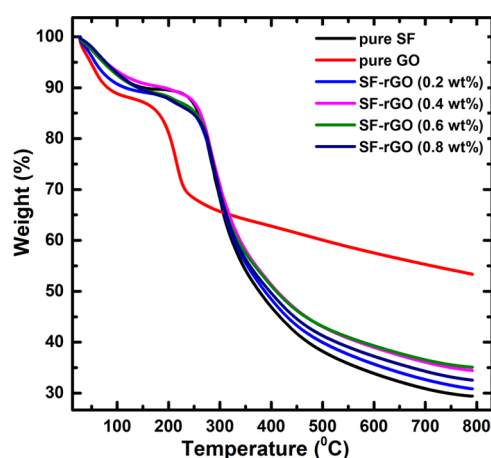
weight loss was observed in the temperature range of 205−450 °C, wherein nearly 50% of the film sample gets decomposed. This weight loss may be because of the interruption of the side chains of the SF macromolecule, which is accountable for the conversion of the GO to rGO nanosheets in the host polymer. Here, the GO showed three stages of weight loss. In the first stage, at a room temperature of 132 °C, about 12.5%, in the second stage (132−210 °C), ∼30%, and in the third stage (210−800 °C), ∼50−65% weight loss was observed. The observed mass losses are attributed to the removal of the water molecules, the thermal decomposition of the groups containing the oxygen molecules, and the decomposition of some unstable carbons present in the structure forming CO and CO_2.[56] After the addition of the GO to the SF, the BNC samples (SF−rGO) showed similar TGA curves with improved thermal stability. In the first stage, the weight loss of ∼10% was observed from laboratory temperature to 195 °C, which may be because of the water loss in the BNCs. The significant weight loss in the next stage (200−450 °C) is related to the interruption of the side-chain groups of the amino acids and the cleavage of the peptide bonds.[57] Nearly about 55−70% of the sample is degraded in the last stage. However, in comparison with the native SF curve, BNCs show improved thermal stability at higher temperature because the GO can stabilize the composite films. This may be due to the strong interaction between the SF and the rGO nanosheets. Moreover, the enhanced silk-II or β-sheet structure provided synergetic effects to increase the thermal stability of the BNCs.
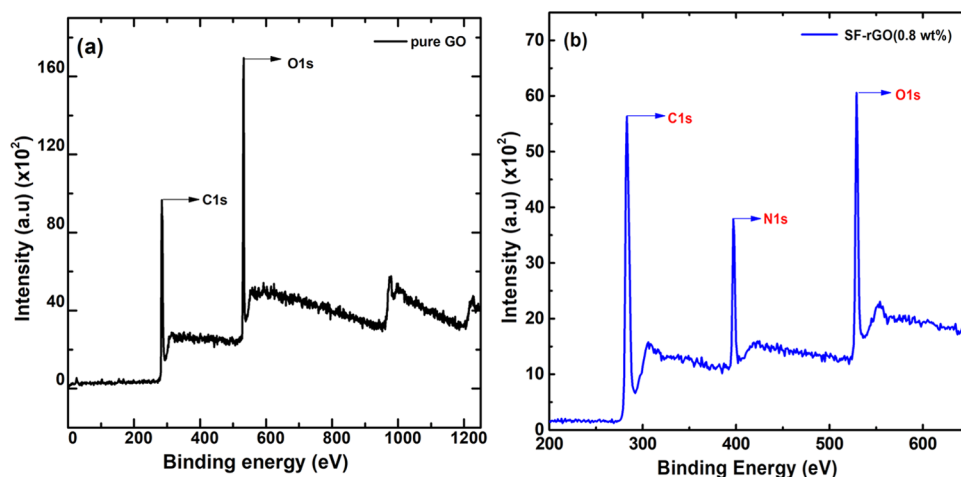
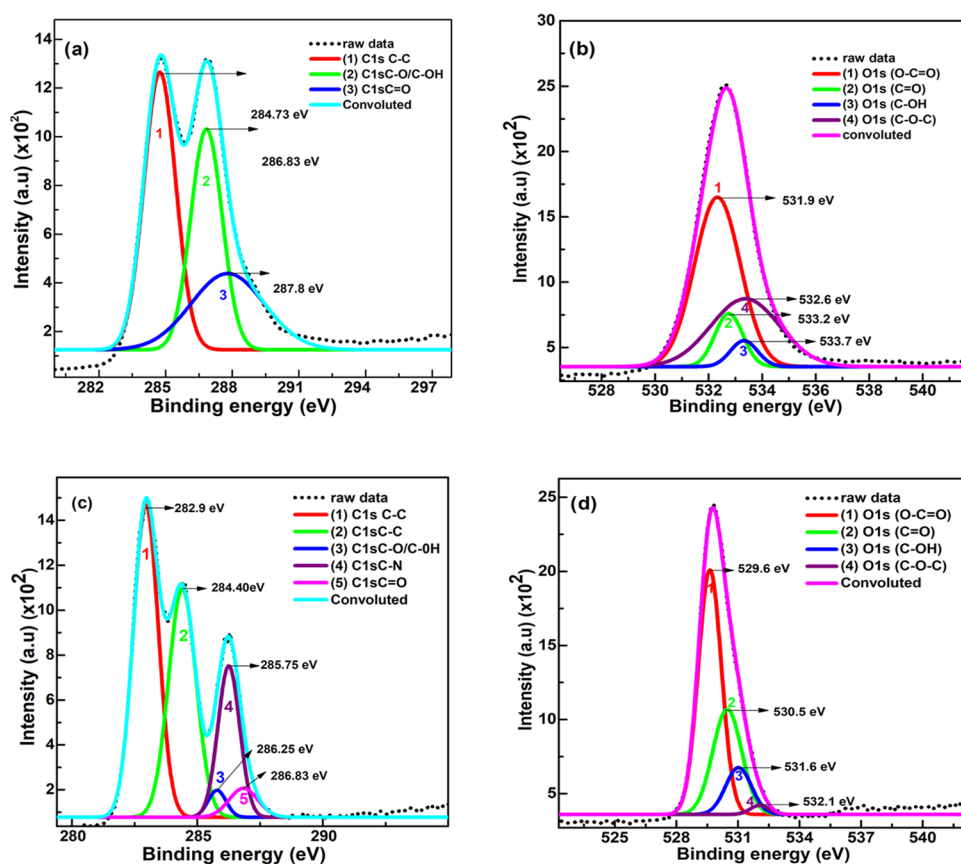**Figure 8.** XPS spectra of (a) pristine GO and (b) SF−rGO.

Figure 9. Deconvolution of the C 1s and O 1s spectra of GO (a, b) and SF−rGO (c, d).

2.7. XPS Analysis. The synthesized GO and the developed SF−rGO BNCs were further studied by XPS to evaluate the chemical composition and the existence of the functional groups. The survey scans of the XPS spectra of the GO and SF−rGO are given in Figure 8a,b. The XPS survey spectrum of the GO clearly indicates the presence of C 1s and O 1s peaks in the sample.[58] The C 1s peak was found to be at a binding energy (BE) of 284.2 eV and the O 1s peak at 531.4 eV. On the other hand, the SF−rGO BNC sample showed similar peaks with an additional peak at a binding energy of 397 eV corresponding to N 1s.[59] Further, it was noticed that the intensity of O 1s was greatly reduced in the BNC sample,

suggesting that the functional groups containing oxygen molecules were partially eliminated.[60]

In order to acquire more information regarding the functional groups in the XPS, the C 1s peaks of both the GO and rGO samples were de-convoluted (Figure 9a−d) into three chemically shifted bands with BEs 282.94, 284.40, and 285.78 eV, representing the three types of carbon-encompassing species.

The peaks observed at BEs 284.43, 286.27, and 288.88 eV correspond to the C−C, C−O, and C=O functional groups.[61] In accordance with the reported literature, the GO has peaks at 284.6, 286.6, and 288.5 eV assigned to the sp^2 carbon, the
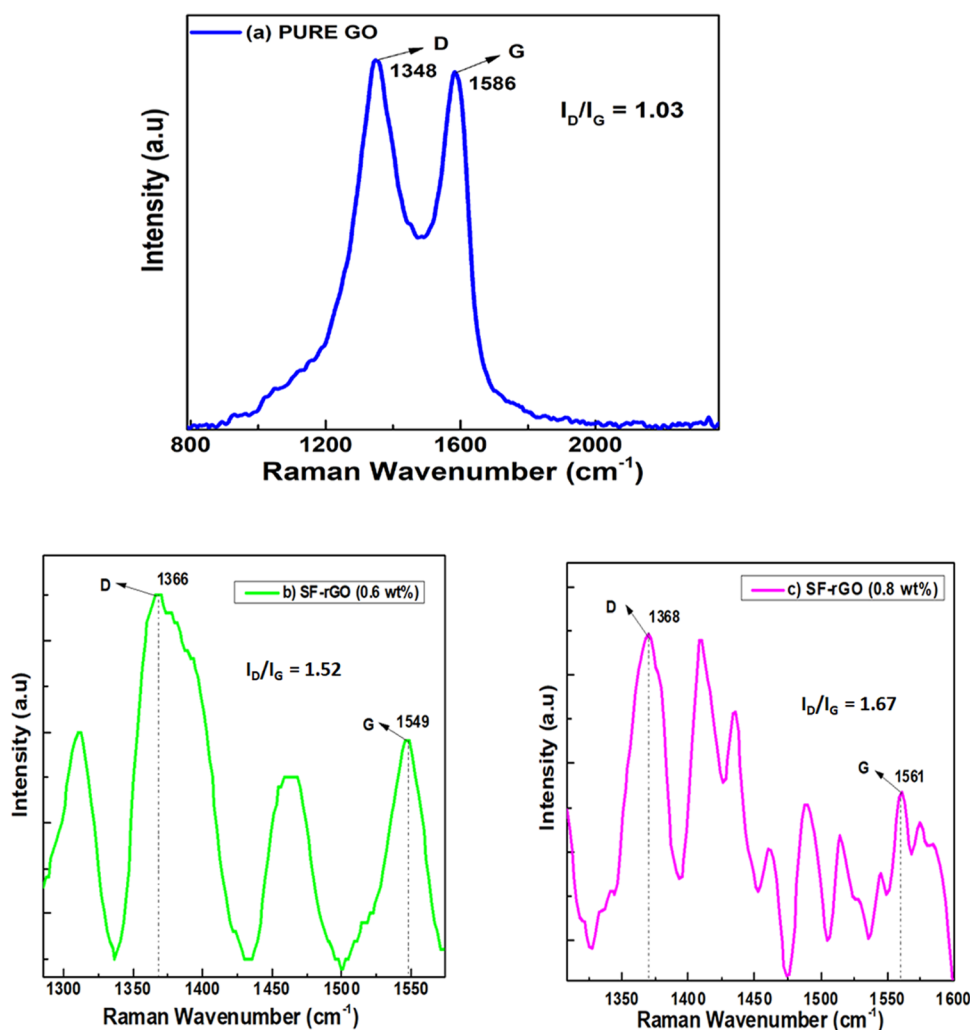
Figure 10. (a) Raman spectra of as-prepared graphite oxide (GO) and (b, c) SF−rGO bionanocomposite films.

epoxide, and carboxyl functional groups, respectively.[62,63] In XPS, the O 1s peak of both the GO and rGO are deconvoluted into chemically shifted bands with BEs 529.63, 530.47, 531.05, and 532.06 eV demonstrating the four types of oxygen species. The slight band shifting of the BNC sample toward lower BEs suggests the formation of reduced GO in the host polymer matrix.[60] This is also supported by other experiments in the study.

2.8. Raman Spectroscopy Study. Raman spectroscopy is normally employed to characterize the graphene and to determine the number of layers.[64,65] The typical Raman spectra of carbon-containing materials show the number of bands and are labelled as D, G, and 2G.[66] The D band arises from the presence of vacancies or dislocation in the graphene layer. It indicates the presence of defects in the sample and is located near the wavenumber 1350 cm^{-1}.[67] The band G appeared near to the wavenumber 1580 cm^{-1} and is related to the in-plane vibration of sp^2 hybridized carbon atoms.[68] The peak 2D is sometimes also referred to as G′ and is associated with the number of graphene layers present in the sample. Also, additional information about the carbon materials can be obtained by analyzing the intensity ratio of the D peak to the G peak (I_D/I_G), which reveals the amount of defects present in the materials.[69] The ratio I_{2D}/I_D provides information

regarding the number of graphene layers present in the materials.[70]

The Raman spectra of the prepared GO and *in situ* reduced graphene oxide samples are presented in Figure 10. Figure 10 shows the Raman peaks' D and G bands at 1348 and 1586 cm^{-1}, respectively. The large intensity of the D band relative to that of the G band indicates the higher amount of the disordered phase in GO. The intensity ratio of the D peak to the G peak (I_D/I_G) was calculated and found to be 1.036, which suggested the oxidation of graphite and is related to the formation of sp^3 hybridized bonds.[71]

On the other hand, after the oxidation of the graphene, the D and G bands in the bionanocomposite were shifted and found to be 1366 and 1549 cm^{-1} in the case of the 0.6 wt % GO (Figure 11a) added sample. In the case of the 0.8 wt % added sample, D and G bands appeared at 1368 and 1561 cm^{-1} (Figure 11b), respectively. The intensity ratio (I_D/I_G) was observed to be 1.52 and 1.67, respectively. The increase in intensity in the SF−rGO bionanocomposite samples may be due to the increased number of sp^2 domains formed during the *in situ* reduction process. It could also be due to the presence of unrepaired defects that remain after the removal of large amounts of oxygen-containing functional groups.[72] These observed results confirm the SF as a reduction agent to reduce GO to rGO.
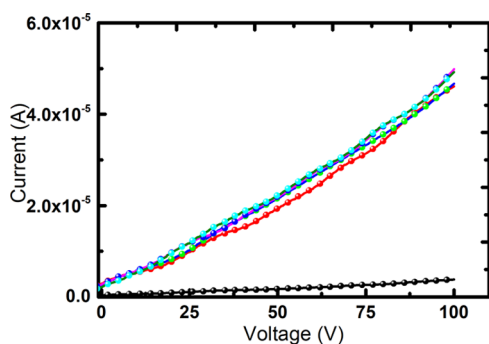
Figure 11. Current−voltage curves of SF−rGO BNCs with the concentration of GO.

2.9. Electrical Properties of the BNC Films. Electrical characterization (DC) of the SF−rGO BNCs was performed to understand the effect of the *in situ* reduced graphene oxide nanosheets in the host matrix. The BNC samples were prepared by adding GO to the SF in different concentrations (0.2, 0.4, 0.6, and 0.8 wt %). The following relation was used to calculate the DC electrical conductivity of the BNCs[73]

$$\sigma_{DC} = \frac{d}{RA} \tag{3}$$

where d represents the thickness, R is the resistance of the sample, and A is the electrode area. The $I-V$ curves of the BNCs with various concentrations of GO at room temperature are presented in Figure 12. It can be noted that the current
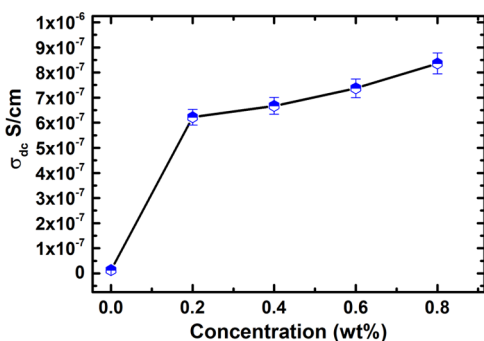
Figure 12. Variation in DC conductivity of SF−rGO BNCs with concentration of GO.

value increases with the increase in applied voltage. The DC electrical conductivity of the BNCs with the varied amounts of GO content was calculated and is tabulated in Table 2. From the table and Figure 13, one can notice the gradually increasing electrical conductivity of the BNCs due to the *in situ* formation of rGO in the SF polymer. The increase of electrical conductivity of the bionanocomposite films may be due to

Table 2. DC Conductivity Values of the SF−rGO BNC Film

sample	current ($\times 10^{-2}$ mA)	resistance ($\times 10^{6}$ Ω)	DC conductivity ($\times 10^{-9}$ S/cm)
pure SF	0.043	118.3	1.28
SF + 0.2 wt % GO	2.01	2.51	62.1
SF + 0.4 wt % GO	2.05	2.46	65.3
SF + 0.6 wt % GO	2.10	2.39	71.8
SF + 0.8 wt % GO	2.23	2.26	82.4

their high rGO nanosheet content and uniform layered structure.

The uniformly dispersed rGO nanosheets greatly improve the conductivity of the SF−rGO nanocomposites probably because of the creation of conductive networks throughout the host polymer matrix. This provides a conducting path in the SF and thus, one can notice increased conductivity. It is also found that the resistance offered by the BNCs decreases with the varied GO content in the SF. This may be due to the reduced distance between the nanosheets. In the reduced-distance situation, the electric field induced is enough for the electrons to tunnel from one nanosheet to another. Thus, enhanced electrical conductivity of the BNCs is achieved in the study. A thorough understanding of the conduction properties of this type of BNCs can make them very useful for biological applications in biosensors and the tissue engineering field.[19,74]

3. CONCLUSIONS

In this work, graphene oxide to reduced graphene oxide nanosheets in the SF biopolymer were realized, and highly conductive BNCs were successfully developed. The used biopolymer acts as a reduction agent for fabricating the reduced graphene oxide nanosheets. The UV−visible spectroscopy study confirmed the synthesis of graphene oxide and the reduced graphene oxide in the silk fibroin by showing plasmon resonance bands. The XRD study revealed the synthesis of graphene oxide using graphite powder, and the reduction of graphene oxide to reduced graphene oxide in the host matrix. The SEM pictures corroborated that the *in situ* formed reduced GO nanosheets were well distributed within the SF matrix. The increasing amount of rGO content in the SF showed the increase of the surface roughness of the BNCs. From the XPS study, it was observed that the oxygen-containing functional groups were partially removed. The Raman spectroscopy showed that the increase in intensity in the SF−rGO bionanocomposite samples may be attributed to the increased number of sp^2 domains formed during the *in situ* reduction process. The $I-V$ characteristics showed that the electrical conductivity of the BNCs continuously increased with the increase in rGO nanosheet content. The high value of conductivity may be due to the large surface area of the *in situ* formed rGO nanosheets in the SF matrix. The successful development of novel conducting SF−rGO bionanocomposite samples will provide favorable opportunities in biosensors, tissue engineering, and many other areas.

4. EXPERIMENTAL SECTION

4.1. Materials. The silkworm (*B. mori*) CB-Gold cocoons were provided by the Sericulture Department, University of Mysore, Mysuru, India. The graphite fine powder (particle size −60 meshes and purity of 98%) was obtained from Lobo Chemie India. Sodium carbonate (Na$_2$CO$_3$ (>99%)), lithium bromide (LiBr (>99%)), concentrated sulfuric acid (98% H$_2$SO$_4$), potassium permanganate (KMnO$_4$), sodium nitrate (NaNO$_3$), and hydrogen peroxide (30% H$_2$O$_2$) were procured from Sigma Aldrich Chemicals Pvt. Ltd., India. All the purchased chemicals were of analytical grade and utilized as received without any modification. Double distilled water was used to prepare all the aqueous solutions in the work.

4.2. Removal of Sericin and Extraction of Silk Fibroin from Silk Cocoons. To remove the sericin, silkworm (*B. mori*) CB-Gold cocoons were cut into small pieces. Then, the

cocoon pieces were chemically degummed by boiling two times with 0.02 M Na_2CO_3 solution at 95 °C for exactly 30 min. Subsequently, the sericin-free SF fiber was washed and cooled by rinsing with double distilled water and then dried.[75−79] The degummed SF fiber was dissolved in 9.3 M aqueous LiBr solution at 60 °C for ∼4 h. The obtained SF solution was then cooled and filled in a dialysis cassette with MWCO 3500 Da (Slide-A-Lyzer: Thermo Fisher Scientific), followed by dialysis against de-ionized water for 3 days at room temperature to eliminate the residual salts. The dialyzed clear SF solution was centrifuged for 20 min at 9000 rpm to eliminate the silk accumulation, if any had occurred during the process. The extracted SF solution was preserved at 4 °C for further study.

4.3. Synthesis of Graphene Oxide. Graphene oxide (GO) was prepared from natural graphite powder using the modified Hummer's method.[80−83] The thermal treatment to the graphite powder solution involved both oxidation and exfoliation during the synthesis of GO. In brief, graphene powder (2 g) and $NaNO_3$ (1 g) were added into 50 mL of 98% concentrated H_2SO_4 in an ice bath under vigorous stirring for 2 h, following which the total mass got converted to a black slurry. Then, 6 g of $KMnO_4$ was slowly added into the slurry, keeping the reaction temperature less than 15 °C, and continuously stirred for 4 h in an ice bath. Afterward, 100 mL of DI water was added to the solution, and the stirring was continued for another 2 h at 70−80 °C. To terminate the reaction and control the pH of the reaction medium, 200 mL of hot water (60 °C), followed by 20 mL of H_2O_2, was added to the above solution. This resulted in a color change from brownish black to bright yellow. The obtained mixture was washed a number of times with DI water, and then the residue was centrifuged. The acquired product was then dried using a hot air oven at 60 °C for 24 h, and the pure graphene oxide powder was collected and used for further experiment.

4.4. Reduction of GO and Preparation of SF−rGO Bionanocomposite Films. For the preparation of bionanocomposites, a known amount of synthesized GO (0.2, 0.4, 0.6, and 0.8 wt %) was mixed with the SF solution. Further, the pH (9−10) of the mixture solution was carefully maintained by using NaOH to avoid aggregation of the SF molecules. The mixture solution was stirred for 20 min and heated in a hot air oven for ∼1 h at 90 °C. Then, the solution was cooled to room temperature and sonicated for about 20 min to obtain uniform distribution of the GO nanosheets. The resulting solution was kept for a few hours to attain suitable viscosity, and subsequently cast onto clean Petri dishes and dried at laboratory temperature. The developed SF−rGO BNC films were peeled carefully and desiccated to avoid moisture. A screw gauge was used to measure the thickness of the samples, which was found to be 60 μm.

4.5. Material Characterization. In ultraviolet−visible absorption study, the optical absorption spectra of the native SF, GO, and SF−rGO in aqueous medium were collected with a Shimadzu UV-1800 (Japan) UV−vis spectrophotometer over a wavelength range of 200−800 nm. The X-ray diffraction patterns of the graphite, GO, and SF−rGO materials were recorded using a Miniflex-II (Rigaku, Japan) diffractometer at laboratory temperature operated at 25 kV and a current of 35 mA using Cu Kα rays (λ = 1.5406 Å). The XRD patterns of the samples were scanned between 5 and 90° (2θ values). The surface morphologies of the native SF, GO, and SF−rGO BNCs were observed under a scanning electron microscope

(SEM) (JSM-6390LV, JEOL, Japan) at an operating voltage of 15 kV. The layered structure of the GO and rGO nanosheets was investigated using a high-resolution transmission electron microscope (HR-TEM) JOEL-JEM 2100 instrument at an accelerating voltage of 200 kV. The suspension of GO and rGO samples (10 μL) was dropped on a carbon-coated copper grid and allowed to dry at room temperature prior to HR-TEM analysis. The mechanical properties of the native SF and SF−rGO BNC samples were measured according to ASTM D882 standard using the universal testing machine (ZwickRoellZ020, Germany). The conditions for analysis of native and BNC films were 25 °C temperature and 65% humidity. The tests of the samples were conducted using a load cell of 5 kN. The film specimens were cut into a rectangular shape (80 mm × 20 mm × 0.06 mm) and held between two clamps positioned at a distance of 50 mm. The measurements of the samples were carried out at a rate of 20 mm/min. The thermal stability study of the SF, GO, and SF−rGO BNCs was carried out under dry nitrogen gas flow (100 mL/min) using a thermogravimetric analyzer (TGA) instrument (TA SDT Q600). The samples were heated from laboratory temperature (27 °C) to 800 °C at a scanning rate of 10 °C/min. The X-ray photoelectron spectroscopy (XPS) was performed using a Kratos axis ultra-X-ray photoelectron spectrometer with a monochromatic aluminum Kα X-ray radiation (1486.6 eV) source. The Raman scans for all of the samples were recorded using XploRA PLUS Raman microscopy (Horiba, Japan). The current−voltage (*I−V*) studies of the SF−rGO BNC films were performed using the two-probe Keithley 5110 digital electrometer at room temperature. The film samples were laid between the Keithley 8009 resistivity text fixtures with computer interface. The electrical conductivity studies were carried out in the voltage range of 0−100 V in multiple steps of 5 V.

■ AUTHOR INFORMATION

Corresponding Author

Sangappa Yallappa − *Department of Studies in Physics, Mangalore University, Mangalore 574 199, Karnataka, India;* ⊙ orcid.org/0000-0001-6633-9101; Phone: +91-9845205065; Email: sangappay@gmail.com; Fax: +91-(0)824-2287367

Authors

Parushuram Nilogal − *Department of Studies in Physics, Mangalore University, Mangalore 574 199, Karnataka, India*

Gauthama B. Uppine − *Department of Chemistry, Mangalore University, Mangalore 574 199, Karnataka, India*

Ranjana Rayaraddi − *Department of Studies in Physics, Mangalore University, Mangalore 574 199, Karnataka, India;* ⊙ orcid.org/0000-0002-5692-3416

Harisha K. Sanjeevappa − *Department of Studies in Physics, Mangalore University, Mangalore 574 199, Karnataka, India*

Lavita J. Martis − *Department of Studies in Physics, Mangalore University, Mangalore 574 199, Karnataka, India*

Badiadka Narayana − *Department of Chemistry, Mangalore University, Mangalore 574 199, Karnataka, India*

Complete contact information is available at:
https://pubs.acs.org/10.1021/acsomega.1c00013

■ REFERENCES

(1) Ghorbanian, J.; Emadi, R.; Razavi, S. M.; Shin, H.; Teimouri, A. Fabrication and characterization of novel diopside/silk fibroin nanocomposite scaffolds for potential application in maxillofacial bone regeneration. *Int. J. Biol. Macromol.* **2013**, *58*, 275−280.

(2) Lin, N. N.; Cao, L.; Huang, Q. Q.; Wang, C.; Wang, Y.; Zhou, J.; Liu, X. Y. Functionalization of silk fibroin materials at mesoscale. *Adv. Funct. Mater.* **2016**, *26*, 8885−8902.

(3) Kwak, H. W.; Ju, J. E.; Shin, M.; Holland, C.; Lee, K. H. Sericin promotes fibroin silk-i stabilization across a phase-separation. *Biomacromolecules* **2017**, *18*, 2343−2349.

(4) Kundu, B.; Rajkhowa, R.; Kundu, S. C.; Wang, X. Silk fibroin biomaterials for tissue regenerations. *Adv. Drug Delivery Rev.* **2013**, *65*, 457−470.

(5) Lawrence, B. D.; Cronin-golomb, M.; Georgakoudi, I.; Kaplan, D. L.; Omenetto, F. G. Bioactive silk protein biomaterial systems for optical devices. *Biomacromolecules* **2008**, *9*, 1214−1220.

(6) Cao, Z.; Chen, X.; Yao, J.; Huang, L.; Shao, Z. The preparation of regenerated silk fibroin microspheres. *Soft Matter* **2007**, *3*, 910−915.

(7) Srisuwan, Y.; Srihanam, P.; Baimark, Y. Preparation of silk fibroin microspheres and its application to protein adsorption. *J. Macromol. Sci., Part A: Pure Appl. Chem.* **2009**, *46*, 521−525.

(8) Hopkins, A. M.; De Laporte, L.; Tortelli, F.; Spedden, E.; Staii, C.; Atherton, T. J.; Hubbell, J. A.; Kaplan, D. L. Silk hydrogels as soft substrates for neural tissue engineering. *Adv. Funct. Mater.* **2013**, *23*, 5140−5149.

(9) Boni, B. O. O.; Lamboni, L.; Bakadia, B. M.; Hussein, S. A.; Yang, G. Combining silk sericin and surface micropatterns in bacterial cellulose dressings to control fibrosis and enhance wound healing. *Eng. Sci.* **2020**, *10*, 68−77.

(10) Kujala, S.; Mannila, A.; Karvonen, L.; Kieu, K.; Sun, Z. Natural silk as a photonics component: a study on its light guiding and nonlinear optical properties. *Sci. Rep.* **2016**, *6*, No. 22358.

(11) Melucci, M.; Durso, M.; Favaretto, L.; Capobianco, M. L.; Benfenati, V.; Sagnella, A.; Ruani, G.; Muccini, M.; Zamboni, R.; et al. Silk doped with a bio-modified dye as a viable platform for eco-friendly luminescent solar concentrators. *RSC Adv.* **2012**, *2*, 8610−8613.

(12) Kim, D. H.; Kim, Y. S.; Amsden, J.; Panilaitis, B.; Kaplan, D. L.; Omenetto, F. G.; Zakin, M. R.; Rogers, J. A. Silicon electronics on silk as a path to bioresorbable, implantable devices. *Appl. Phys. Lett.* **2009**, *95*, No. 133701.

(13) Zheng, Z.; Olayinka, O.; Li, B. 2S-soy protein-based biopolymer as a non-covalent surfactant and its effects on electrical conduction and dielectric relaxation of polymer nanocomposites. *Eng. Sci.* **2018**, *4*, 87−99.

(14) Dong, Q.; Wang, X.; Liu, H.; Ryu, H.; Zhao, J.; Li, B.; Lei, Y. Heterogeneous iridium oxide/gold nanocluster for non-enzymatic glucose sensing and pH probing. *Eng. Sci.* **2019**, *8*, 46−53.

(15) Huang, Y.; Luo, Y.; Liu, H.; Lu, X.; Zhao, J.; Lei, Y. A Subcutaneously injected SERS nanosensor enabled long-term in vivo glucose tracking. *Eng. Sci.* **2021**, *14*, 59−68.

(16) Huang, H.; Han, L.; Wang, Y.; Yang, Z.; Zhu, F.; Xu, M. Tunable thermal-response shape memory bio-polymer hydrogels as body motion sensors. *Eng. Sci.* **2019**, *9*, 60−67.

(17) Chen, J.; Zhu, Y.; Guo, Z.; Nasibulin, A. G. Recent progress on thermo-electrical properties of conductive polymer composites and their application in temperature sensors. *Eng. Sci.* **2020**, *12*, 13−22.

(18) Su, Y. F.; Han, G.; Kong, Z.; Nantung, T.; Lu, N. Embeddable piezoelectric sensors for strength gain monitoring of cementitious materials: the influence of coating materials. *Eng. Sci.* **2020**, *11*, 66−75.

(19) Reizabal, A.; Goncalves, S.; Brito-Pereira, R.; Costa, P.; Costa, C. M.; Pérez-Álvarez, L.; Vilas-Vilela, J. L.; Lanceros-Méndez, S. Optimized silk fibroin piezoresistive nanocomposites for pressure sensing applications based on natural polymers. *Nanoscale Adv.* **2019**, *1*, 2284−2292.

(20) Zhang, H.; Zhao, J.; Xing, T.; Lu, S.; Chen, G. Fabrication of silk fibroin/graphene film with high electrical conductivity and humidity sensitivity. *Polymers* **2019**, *11*, No. 1774.

(21) Jia, X.; Wang, C.; Ranganathan, V.; Napier, B.; Yu, C.; Chao, Y.; Forsyth, M.; F. Omenetto, F. G.; Macfarlane, D. R.; Wallace, G. G. A biodegradable thin-film magnesium primary battery using silk fibroin-ionic liquid polymer electrolyte. *ACS Energy Lett.* **2017**, *2*, 831−836.

(22) Pal, R. K.; Farghaly, A. A.; Collinson, M. M.; Kundu, S. C.; Yadavalli, V. K. Photolithographic micropatterning of conducting polymers on flexible silk matrices. *Adv. Mater.* **2016**, *28*, 1406−1412.

(23) Jian, M.; Wang, C.; Wang, Q.; Wang, H.; Xia, K.; Yin, Z.; Zhang, M.; Liang, X.; Zhang, Y. Advanced carbon materials for flexible and wearable sensors. *Sci. China Mater.* **2017**, *60*, 1026−1062.

(24) Wang, C.; Xia, K.; Zhang, Y.; Kaplan, D. L. Silk-based advanced materials for soft electronics. *Acc. Chem. Res.* **2019**, *52*, 2916−2927.

(25) Wang, Y.; Shi, Z. X.; Yin, J. Facile synthesis of soluble graphene via a green reduction of graphene oxide in tea solution and its biocomposites. *ACS Appl. Mater. Interfaces* **2011**, *3*, 1127−1133.

(26) Zhu, Q.; Liu, J.; Wang, X.; Huang, Y.; Ren, Y.; Song, W.; Mu, C.; Liu, X.; Wei, F.; Liu, C. Polypyrrole functionalized graphene oxide accelerated zinc phosphate coating under low-temperature. *ES Mater. Manuf.* **2020**, *9*, 48−54.

(27) Tang, C.; Yu, X.; Li, G.; Yang, N.; Lü, J. Phonon thermal transport properties of graphene periodically embedded with four-and eight-membered rings: a molecular dynamics study. *ES Mater. Manuf.* **2018**, *3*, 16−21.

(28) Li, J.; Zhang, P.; He, H.; Zhai, S.; Xian, Y.; Ma, W.; Wang, L. Enhanced thermal transport properties of epoxy resin thermal interface materials. *ES Energy Environ.* **2019**, *4*, 41−47.

(29) Phiri, J.; Johansson, L. S.; Gane, P.; Maloney, T. A comparative study of mechanical, thermal and electrical properties of graphene, graphene oxide and reduced graphene oxide-doped microfibrillated cellulose nanocomposites. *Composites, Part B* **2018**, *147*, 104−113.

(30) Singh, R. K.; Kumar, R.; Singh, D. P. Graphene oxide: strategies for synthesis, reduction and frontier applications. *RSC Adv.* **2016**, *6*, 64993−65011.

(31) Lee, C.; Wei, X.; Kysar, J. W.; Hone, J. Measurement of the elastic properties and intrinsic strength of monolayer graphene. *Science* **2008**, *321*, 385−388.

(32) Zhou, Y.; Wang, P.; Ruan, G.; Xu, P.; Ding, Y. Synergistic effect of P [MPEGMA-IL] modified graphene on morphology and dielectric properties of PLA/PCL blends. *ES Mater. Manuf.* **2021**, *11*, 20−29.

(33) Wu, X.; Liu, R. Near-field radiative heat transfer between graphene covered biaxial hyperbolic materials. *ES Energy Environ.* **2020**, *10*, 66−72.

(34) Wu, N.; Bai, X.; Pan, D.; Dong, B.; Wei, R.; Naik, N.; Patil, R. R.; Guo, Z. 2021. Recent advances of asymmetric supercapacitors. *Adv. Mater. Interfaces* **2021**, *8*, No. 2001710.

(35) Dong, H.; Li, Y.; Chai, H.; Cao, Y.; Chen, X. Hydrothermal synthesis of $CuCo_2S_4$ nano-Structure and N-doped graphene for high-performance aqueous asymmetric supercapacitors. *ES Energy Environ.* **2019**, *4*, 19−26.

(36) Wei, L.; Lozano, K.; Mao, Y. Microwave popped Co (II)-graphene oxide hybrid: bifunctional catalyst for hydrogen evolution reaction and hydrogen storage. *Eng. Sci.* **2018**, *3*, 62−66.

(37) Li, X.; Zhao, W.; Yin, R.; Huang, X.; Qian, L. A highly porous polyaniline-graphene composite used for electrochemical super-capacitors. *Eng. Sci.* **2018**, *3*, 89−95.

(38) Chen, Y.; Wang, Y.; Su, T.; Chen, J.; Zhang, C.; Lai, X.; Jiang, D.; Wu, Z.; Sun, C.; Li, B.; Guo, Z. Self-healing polymer composites based on hydrogen bond reinforced with graphene oxide. *ES Mater. Manuf.* **2019**, *4*, 31−37.

(39) Fu, Y.; Pei, X.; Dai, Y.; Mo, D.; Lyu, S. Three-dimensional graphene-like carbon prepared from CO_2 as anode material for high-performance lithium-ion batteries. *ES Energy Environ.* **2019**, *4*, 66−73.

(40) Song, P.; Liu, B.; Liang, C.; Ruan, K.; Qiu, H.; Ma, Z.; Guo, Y.; Gu, J. Lightweight, flexible cellulose-derived carbon aerogel@ reduced graphene oxide/PDMS composites with outstanding EMI shielding performances and excellent thermal conductivities. *Nano-Micro Lett.* **2021**, *13*, 1−17.

(41) Wang, L.; Shi, X.; Zhang, J.; Zhang, Y.; Gu, J. Lightweight and robust rGO/sugarcane derived hybrid carbon foams with outstanding EMI shielding performance. *J. Mater. Sci. Technol.* **2020**, *52*, 119−126.

(42) Zhang, Y.; Ruan, K.; Shi, X.; Qiu, H.; Pan, Y.; Yan, Y.; Gu, J. Ti3C2Tx/rGO porous composite films with superior electromagnetic interference shielding performances. *Carbon* **2021**, *175*, 271−280.

(43) Nidamanuri, N.; Li, Y.; Li, Q.; Dong, M. Graphene and graphene oxide-based membranes for gas separation. *Eng. Sci.* **2020**, *9*, 3−16.

(44) Zhao, S.; Niu, M.; Peng, P.; Cheng, Y.; Zhao, Y. Edge oleylaminated graphene as ultra-stable lubricant additive for friction and wear reduction. *Eng. Sci.* **2019**, *9*, 77−83.

(45) Chen, Y.; Guo, Z.; Das, R.; Jiang, Q. Starch-based carbon nanotubes and graphene: preparation, properties and applications. *ES Food Agroforestry* **2020**, *2*, 13−21.

(46) Das, S.; Dhar, B. B. Green synthesis of noble metal nanoparticles using cysteine-modified silk fibroin: catalysis and antibacterial activity. *RSC Adv.* **2014**, *4*, 46285−46292.

(47) Chen, D.; Li, L.; Guo, L. An Environment-friendly preparation of reduced graphene oxide nanosheets via amino acid. *Nanotechnology* **2011**, *22*, No. 325601.

(48) Sadhukhan, S. S.; Ghosh, T. K.; Rana, D.; Roy, I.; Bhattacharyya, A.; Sarkar, G.; Chakraborty, M.; Chattopadhyay, D. Studies on synthesis of reduced graphene oxide (rGO) via green route and its electrical property. *Mater. Res. Bull.* **2016**, *79*, 41−51.

(49) Yang, Y.; Ding, X.; Zou, T.; Peng, G.; Liu, H.; Fan, Y. Preparation and characterization of electrospun graphene/silk fibroin conductive fibrous scaffolds. *RSC Adv.* **2017**, *7*, 7954−7963.

(50) Wang, L.; Lu, C.; Li, Y.; Wu, F.; Zhao, B.; Dong, X. Green fabrication of porous silk fibroin/graphene oxide hybrid scaffolds for bone tissue engineering. *RSC Adv.* **2015**, *5*, 78660−78668.

(51) Pramanik, N.; De, J.; Basu, R. K.; Rath, T.; Kundu, P. P. Fabrication of magnetite nanoparticle doped reduced graphene oxide grafted polyhydroxyalkanoate nanocomposites for tissue engineering application. *RSC Adv.* **2016**, *6*, 46116−46133.

(52) Bouša, D.; Luxa, J.; Mazanek, V.; Jankovsky, O.; Sedmidubsky, D.; Klímova, K.; Pumera, M.; Sofer, Z. Toward graphene chloride: chlorination of graphene and graphene oxide. *RSC Adv.* **2016**, *6*, 66884−66892.

(53) Roy, I.; Bhattacharyya, A.; Sarkar, G.; Saha, N. R.; Rana, D.; Ghosh, P. P.; Palit, M.; Das, A. R.; Chattopadhyay, D. In situ synthesis of a reduced graphene oxide/cuprous oxide nanocomposite: a reusable catalyst. *RSC Adv.* **2014**, *4*, 52044−52052.

(54) Shetty, G. R.; Rao, B. L.; Asha, S.; Wang, Y.; Sangappa, Y. Preparation and characterization of silk fibroin/hydroxypropyl methyl cellulose (hpmc) blend films. *Fibers Polym.* **2015**, *16*, 1734−1741.

(55) Wang, L.; Lu, C.; Zhang, B.; Zhao, B.; Wu, F.; Guan, S. Fabrication and characterization of flexible silk fibroin films reinforced with graphene oxide for biomedical applications. *RSC Adv.* **2014**, *4*, 40312−40320.

(56) Sharma, N.; Sharma, V.; Jain, Y.; Kumari, M.; Gupta, R.; Sharma, S. K.; Sachdev, K. Synthesis and characterization of graphene oxide (go) and reduced graphene oxide (rgo) for gas sensing application. *Macromol. Symp.* **2017**, *376*, No. 1700006.

(57) El Achaby, M.; Arrakhiz, F. Z.; Vaudreuil, S.; Essassi, E. M.; Qaiss, A. Piezoelectric β- polymorph formation and properties enhancement in graphene oxide - pvdf nanocomposite films. *Appl. Surf. Sci.* **2012**, *258*, 7668−7677.

(58) Hanifah, M. F. R.; Jaafar, J.; Othman, M. H. D.; Ismail, A. F.; Rahman, M. A.; Yusof, N.; Salleh, W. N. W.; Aziz, F. Facile synthesis of highly favorable graphene oxide: effect of oxidation degree on the structural, morphological, thermal and electrochemical properties. *Materialia* **2019**, *6*, No. 100344.

(59) Yang, X.; Tu, Y.; Li, L.; Shang, S.; Tao, X. M. Well-dispersed chitosan/graphene oxide nanocomposites. *ACS Appl. Mater. Interfaces* **2010**, *2*, 1707−1713.

(60) Al-Gaashani, R.; Najjar, A.; Zakaria, Y.; Mansour, S.; Atieh, M. A. XPS and structural studies of high quality graphene oxide and reduced graphene oxide prepared by different chemical oxidation methods. *Ceram. Int.* **2019**, *45*, 14439−14448.

(61) Abdulkhani, A. A.; Daliri Sousefi, M.; Ashori, A.; Ebrahimi, G. Preparation and characterization of sodium carboxymethyl cellulose/silk fibroin/graphene oxide nanocomposite films. *Polym. Test.* **2016**, *52*, 218−224.

(62) Cao, J.; Wang, C. Multifunctional surface modification of silk fabric via graphene oxide repeatedly coating and chemical reduction method. *Appl. Surf. Sci.* **2017**, *405*, 380−388.

(63) Aunkor, M. T. H.; Mahbubul, I. M.; Saidur, R.; Metselaar, H. S. C. The green reduction of graphene oxide. *RSC Adv.* **2016**, *6*, 27807−27825.

(64) Kubesa, O.; Horackova, V.; Moravec, Z.; Farka, Z.; Skladal, P. Graphene and graphene oxide for biosensing. *Monatsh. Chem.* **2017**, *148*, 1937−1944.

(65) Kaniyoor, A.; Ramaprabhu, S. A Raman spectroscopic investigation of graphite oxide derived graphene. *AIP Adv.* **2012**, *2*, No. 032183.

(66) Xu, L.; Cheng, L. Graphite oxide under high pressure: a Raman spectroscopic study. *J. Nanomater.* **2013**, *2013*, 1−5.

(67) Ni, Z.; Wang, Y.; Yu, T.; Shen, Z. Raman spectroscopy and imaging of graphene. *Nano Res.* **2008**, *1*, 273−291.

(68) Vecera, P.; Eigler, S.; Kolesnik-Gray, M.; Krstic, V.; Vierck, A.; Maultzsch, J.; Schäfer, R. A.; Hauke, F.; Hirsch, A. Degree of functionalisation dependence of individual Raman intensities in covalent graphene derivatives. *Sci. Rep.* **2017**, *7*, No. 45165.

(69) Nguyen, V. T.; Le, H. D.; Nguyen, V. C.; Ngo, T. T. T.; Nguyen, X. N.; Phan, N. M. Synthesis of multi-layer graphene films on copper tape by atmospheric pressure chemical vapour deposition method. *Adv. Nat. Sci.: Nanosci. Nanotechnol.* **2013**, *4*, No. 035012.

(70) Muzyka, R.; Drewniak, S.; Pustelny, T.; Chrubasik, M.; Gryglewicz, G. Characterization of graphite oxide and reduced graphene oxide obtained from different graphite precursors and oxidized by different methods using Raman spectroscopy. *Materials* **2018**, *11*, No. 1050.

(71) Narita, C.; Okahisa, Y.; Wataoka, I.; Yamada, K. Characterization of ground silk fibroin through comparison of nanofibroin and higher order structures. *ACS Omega* **2020**, *5*, 22786−22792.

(72) Meti, S.; Rahman, M. R.; Ahmad, M. I.; Bhat, K. U. Chemical free synthesis of graphene oxide in the preparation of reduced graphene oxide-zinc oxide nanocomposite with improved photo-catalytic properties. *Appl. Surf. Sci.* **2018**, *451*, 67−75.

(73) Ranjana, R.; Parushuram, N.; Harisha, K. S.; Asha, S.; Narayana, B.; Mahendra, M.; Sangappa, Y. Fabrication and characterization of conductive silk fibroin−gold nanocomposite films. *J. Mater. Sci.: Mater. Electron.* **2020**, *31*, 249−264.

(74) Ciszewski, M.; Benke, G.; Leszczyńska-Sejda, K.; Kopyto, D. Facile synthesis of reduced graphene oxide/peroxomolybdate(vi)−citrate composite and its potential energy storage application. *Appl. Phys. A: Mater. Sci. Process.* **2017**, *123*, 713.

(75) Sangappa, Y.; Latha, S.; Asha, S.; Sindhu, P.; Parushuram, N.; Shilpa, M.; Byrappa, K.; Narayana, B. Synthesis of anisotropic silver nanoparticles using silk fibroin: characterization and antimicrobial properties. *Mater. Res. Innovations* **2017**, *23*, 79−85.

(76) Parushuram, N.; Asha, S.; Suma, S. B.; Krishna, K.; Neelakandan, R.; Sangappa, Y. Green synthesis of high yield mono-dispersed gold nanoparticles using silk-sericin and characterization. *AIP Conf. Proc.* **2019**, *2142*, No. 150016.

(77) Ranjana, R.; Parushuram, N.; Harisha, K. S.; Asha, S.; Sangappa, Y. Silk fibroin a bio-template for synthesis of different shaped gold nanoparticles: characterization and ammonia detection application. *Mater. Today: Proc.* **2020**, *27*, 434−439.

(78) Lakshmeesha Rao, B.; Gowda, M.; Asha, S.; Byrappa, K.; Narayana, B.; Somashekar, R.; Wang, Y.; Madhu, L. N.; Sangappa, Y. Rapid synthesis of gold nanoparticles using silk fibroin: character-ization, antibacterial activity, and anticancer properties. *Gold Bull.* **2017**, *50*, 289−297.

(79) Asha, S.; Sangappa, Y.; Sanjeev, G. Tuning the refractive index and optical band gap of silk fibroin films by electron irradiation. *J. Spectrosc.* **2015**, 1−7.

(80) Chen, J.; Li, Y.; Huang, L.; Li, C.; Shi, G. High-yield preparation of graphene oxide from small graphite flakes via an improved hummers method with a simple purification process. *Carbon* **2015**, *81*, 826−834.

(81) Wang, X.; Bai, H.; Yao, Z.; Liu, A.; Shi, G. Electrically conductive and mechanically strong biomimetic chitosan/reduced graphene oxide composite films. *J. Mater. Chem.* **2010**, *20*, 9032−9036.

(82) Wang, J.; Salihi, E. C.; Siller, L. Green reduction of graphene oxide using alanine. *Mater. Sci. Eng., C* **2017**, *72*, 1−6.

(83) Zaaba, N. I.; Foo, K. L.; Hashim, U.; Tan, S. J.; Liu, W. W.; Voon, C. H. Synthesis of graphene oxide using modified hummers method: solvent influence. *Procedia Eng.* **2017**, *184*, 469−477.